Source effects in higher-order ambient seismic field correlations

Sven Schippkus[1], Gregor Hillers[2], Céline Hadziioannou[1]

[1]Institute of Geophysics, University of Hamburg, Germany

[2]Institute of Seismology, Department of Geosciences and Geography, University of Helsinki, Finland

Key Points:

- Higher-order correlations facilitate the use of asynchronous station recordings and can enhance correlation functions for imaging.
- The re-correlation of direct waves increases the sensitivity to source effects which can lead to significant velocity estimation errors.
- The limited availability of "virtual sources" for re-correlation can introduce additional velocity bias.

This manuscript has been revised after peer review and is currently under consideration for publication at Journal of Geophysical Research: Solid Earth.

Corresponding author: Sven Schippkus, `sven.schippkus@uni-hamburg.de`

Abstract

Seismic interferometry of the ambient seismic field is widely used for surface wave imaging. It typically requires synchronous station recordings and assumes uniform noise source distributions. Higher-order correlations, such as the re-correlation of direct waves (C_2), enable imaging with asynchronous data and have been shown to improve an incomplete source distribution. Using field data and simulations, we show, however, that C_2 surface wavefields are highly sensitive to the original source distribution and even amplify the effects associated with strong directional incidence. This can lead to systematic errors in the obtained velocity estimates and the downstream subsurface images. Tested strategies for selecting auxiliary stations in the re-correlation process do not mitigate this bias but can introduce additional wavefield distortions. Local and far-field imaging approaches using higher-order C_2 correlation wavefields are affected by significant and systematic velocity estimation errors. Our results show that the re-correlation of direct waves is not an all-purpose correlation wavefield enhancement technique, and highlight the need for a careful consideration of source effects for improved imaging.

Plain Language Summary

Seismic interferometry is a technique that uses background vibrations, or "ambient seismic noise", to create images of the Earth's subsurface. Traditionally, this method works best when all sensors record ground vibrations at the same time and when the noise sources are spread out evenly. A derived technique referred to as higher-order correlation has been applied to allow imaging with data from sensors that were not recording at the same time, and to better handle uneven noise source distributions. Using field data and wavefield simulations, we however find that these higher-order techniques do not reduce the problems caused by uneven or isolated noise sources. In fact, they can amplify these problems, leading to significant errors in estimates of structural properties. Hence if source effects are not carefully studied and accounted for, the application of higher-order correlations can result in systematically biased subsurface images.

Keywords: Surface waves and free oscillations, Time series analysis, Wave propagation, Theory, Tomography

1 Introduction

The ambient seismic field is routinely used to image and monitor Earth structure (Shapiro et al., 2005; Sens-Schönfelder & Wegler, 2006; Poli et al., 2012; Lu et al., 2018; Mao et al., 2025). Seismic interferometry of this complex wavefield yields a new wavefield—the C_1 correlation wavefield—that is related to the Green's function of the medium when sources are homogeneously distributed or, equivalently, when the illumination is isotropic (Wapenaar et al., 2005; Snieder et al., 2008). For commonly observed heterogeneous source distributions, the C_1 phase and associated travel time estimates are biased (Tsai, 2009; Froment et al., 2010; Wang et al., 2016; Schippkus et al., 2022). Strategies to mitigate this influence include temporal averaging (Sabra et al., 2005), correlation lapse-time averaging (Bensen et al., 2007), correlation lapse-time selection (Schippkus et al., 2022), filtering (Seydoux et al., 2017), jointly inverting for sources and structure (Fichtner et al., 2017; Sager et al., 2020), or excitation pattern based error modeling for potential consideration in the inversion (Giammarinaro et al., 2023).

Higher-order correlations are an alternative data-driven processing strategy for correlation wavefield enhancement (Stehly et al., 2008; Curtis & Halliday, 2010; Froment et al., 2011; Ma & Beroza, 2012; Sheng et al., 2018). Higher-order correlation refers to the re-correlation of C_1 wavefields to obtain a new correlation wavefield with improved characteristics for imaging. For the reconstruction of a regular C_1 function the recordings of two stations are cross-correlated, which we refer to as the receiver station and the master station or "virtual source" (Figure 1a). For a higher-order correlation at least one additional "auxiliary" station is required (Figure 1b). This approach is therefore also referred to as three-station interferometry (S. Zhang et al., 2020). Higher-order correlations can yield improved velocity estimates (S. Zhang et al., 2020; Nouibat et al., 2022). In addition to the imaging enhancement, this strategy facilitates the processing of asynchronously recorded data. This can significantly expand the applicability of seismic noise interferometry to extended configurations under the assumption of constant medium properties (Ma & Beroza, 2012; Chen & Saygin, 2020; S. Zhang et al., 2020).

More generally, higher-order seismic interferometry allows the reconstruction of signals for geometries beyond the receiver-receiver setup we investigate here. "Receiver-receiver" here refers to the reconstruction of a signal that would be emitted by a receiver—the master station or virtual source—and recorded at a second receiver. In contrast, source-receiver

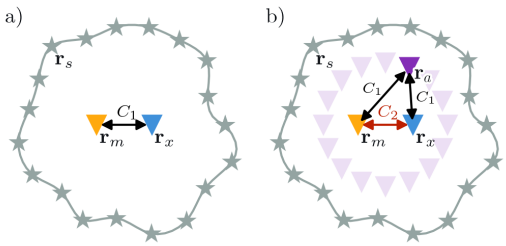

Figure 1. Cross-correlation concepts. (a) The C_1 cross-correlation of the receiver station (blue triangle) and master station (orange triangle) data is proportional to the Green's function $G(\mathbf{r}_x, \mathbf{r}_m)$ for homogeneously distributed noise sources along a boundary (dark gray stars). (b) The higher-order C_2 cross-correlation involves the re-correlation of the direct waves in the two C_1 wavefields between an auxiliary station (purple triangle) and the master and receiver station, respectively. Stacking over homogeneously distributed auxiliary stations is equivalent to a homogeneous virtual source distribution. In that case, C_2 also yields the Green's function $G(\mathbf{r}_x, \mathbf{r}_m)$, but the requirement of simultaneous data acquisition at $\mathbf{r}_x$ and $\mathbf{r}_m$ is relaxed.

interferometry reconstructs signals excited by an actual source such as an earthquake at any location that is not instrumented during the event through iterative interferometry, provided a continuously operating backbone network is available, and the target location is instrumented afterwards (Curtis & Halliday, 2010; Curtis et al., 2012). The reconstruction goal of both approaches is the Green's function between two locations. They differ, however, in that receiver-receiver interferometry commonly relies exclusively on ambient seismic noise as the signal, whereas source-receiver interferometry also requires an isolated source signal, e.g., from an active source (Duguid et al., 2011) or earthquake (Entwistle et al., 2015). Duguid et al. (2011) have shown that iterative interferometry can even enhance the reconstruction of the signal emitted by the active source compared to regular C_1 noise interferometry of two stations placed at the same source and receiver locations.

Higher-order correlations too can yield robust Green's function estimates. The C_2 wavefield is obtained by re-correlating the direct waves in the C_1 wavefields reconstructed with persistent auxiliary stations ($\mathbf{r}_a$ in Figure 1b), whereas the C_3 wavefield results from the re-correlation of the multiple scattered C_1 coda waves. To obtain C_2 Green's functions the locations of auxiliary stations must meet certain requirements. They can be homogeneously distributed, which is equivalent to the ideal situation of an isotropic il-

lumination associated with a homogeneous distribution of original sources for the C_1 Green's function estimate (Figure 1b). Alternatively, auxiliary stations located in the endfire lobes of each master-receiver station pair can achieve the same quality estimates (Entwistle et al., 2015; S. Zhang et al., 2020), again in analogy to C_1 seismic interferometry (Roux et al., 2004; Wapenaar et al., 2010). In contrast, C_3 wavefields approximate the Green's function because the scattered C_1 coda waves impinge on the stations from a wide range of directions (Stehly et al., 2008; Ma & Beroza, 2012). Robust C_3 results can hence be achieved with a significantly smaller number of auxiliary stations compared to C_2 processing, however, the use of several auxiliary stations often support the convergence of stable C_3 estimates (Stehly et al., 2008; Ma & Beroza, 2012; Hillers et al., 2016; Sheng et al., 2018). In contrast to the stochasticity of scatterers, the C_2 approach provides better control on the illumination and the ballistic wave propagation solutions facilitate numerical analysis.

The $C_{1,2,3}$ terminology used here follows Stehly et al. (2008) and Sheng et al. (2018), but different naming conventions have been used (Curtis et al., 2012; S. Zhang et al., 2020). The concepts and jargon used to exchange about higher-order correlations can vary and the obtained results can be counter-intuitive. This includes the view on wavefield directionality. It can be described from a local observational viewpoint based on beamforming or other directional measurements, or it is discussed from the perspective of the distant sources and their distribution. Here we adopt a source centered discussion to develop our arguments (Figures 1, 2, Sections 2, 3) but we frequently make the connection to the local surface wavefield incidence.

The most common subsurface imaging strategy using the ambient seismic field is surface-wave tomography (Shapiro et al., 2005; Lin et al., 2008; Lu et al., 2018; Schippkus et al., 2018; Nouibat et al., 2022), because surface waves tend to dominate the original and hence the C_1 wavefields (Toksöz & Lacoss, 1968; Harmon et al., 2008; Juretzek & Hadziioannou, 2016). For tomography, surface wave group or phase velocity dispersion is measured from the reconstructed Rayleigh and Love propagation in the C_1 wavefield. The obtained frequency-dependent travel times between stations that are separated by at least two wavelengths (Bensen et al., 2007) are then inverted for lateral velocity distributions and 3D shear wave velocity models (Barmin et al., 2001; X. Zhang et al., 2018). An alternative to the inversion of travel times estimated from interstation cross-correlation is the analysis of the spatial auto-correlation (SPAC) (Aki, 1957). In the time

domain the spatial auto-correlation is the focal spot. This is the cross-correlation amplitude field at zero correlation lapse time between a reference station and all other sensors in a dense seismic array. It can be understood to result from the interference of the converging waves that are reconstructed at negative correlation lapse times (Fink, 1999; Derode et al., 2003; Catheline et al., 2008). The Bessel-function shape of a narrowband Rayleigh wave focal spot obtained from vertical component data is governed by the local phase velocity and can thus be used to constrain the velocity structure without solving a tomographic inverse problem. Focal spot imaging can complement tomography because it can extend the resolution of dense array surface wave imaging (Hillers et al., 2016; Giammarinaro et al., 2023, 2024; Tsarsitalidou et al., 2024, 2026).

Here, we investigate how the common observational situation of non-isotropic source distributions affects higher-order correlations. We focus on the C_2 wavefield properties obtained from the re-correlation of direct Rayleigh surface waves and demonstrate with observations and simulations that these higher-order correlations amplify the source signature in the C_1 wavefields. We analyze densely sampled focal spot amplitude patterns because they effectively characterize the C_1 and C_2 correlation wavefield properties and thus help to evaluate the impact of the enhanced source effect. For this, we investigate C_1 wavefield focal spots obtained from field data and simulations (Section 2) and the relationship between the C_1 wavefield source signature and the C_2 wavefield properties (Section 3). We evaluate source effect mitigation strategies (Section 4) and the impact on imaging applications, including focal spot imaging and tomography (Section 5).

2 Cross-correlation of the ambient seismic field (C_1)

First, we study source effects in a C_1 correlation wavefield obtained from vertical component field data and then simulate wavefields to reproduce the observations. We adopt a conceptual framework that discriminates between the original wavefield excitation from boundary sources and isolated sources (Schippkus et al., 2022). Consider the wavefield record u at location $\mathbf{r}_x$ that is induced by a source at $\mathbf{r}_s$. Neglecting an explicit frequency ω dependence, u is

$$u(\mathbf{r}_x) = N_s G(\mathbf{r}_x, \mathbf{r}_s), \tag{1}$$

where N_s is the source spectrum and G the Green's function. The C_1 cross-correlation of the records from the master station at $\mathbf{r}_m$ and a receiver station at $\mathbf{r}_x$ is

$$C_1(\mathbf{r}_x, \mathbf{r}_m) = \langle u(\mathbf{r}_x) u^*(\mathbf{r}_m) \rangle_s \,, \tag{2}$$

where $\langle \cdot \rangle_s$ indicates ensemble averaging over all sources (Wapenaar et al., 2010). If the wavefield is excited by sources that are homogeneously distributed along a boundary S and by one additional isolated noise source at $\mathbf{r}_I$ with source spectrum N_I, the C_1 correlation wavefield is given by (Schippkus et al., 2022, eq. 6)

$$C_1(\mathbf{r}_x, \mathbf{r}_m) = \underbrace{\frac{\rho c |N_s|^2}{2} \big(G(\mathbf{r}_x, \mathbf{r}_m) + G^*(\mathbf{r}_x, \mathbf{r}_m) \big)}_{\text{boundary source contribution}} + \underbrace{G(\mathbf{r}_x, \mathbf{r}_I) G^*(\mathbf{r}_x, \mathbf{r}_I) |N_I|^2}_{\text{isolated source contribution}} . \tag{3}$$

The boundary source contribution to the C_1 wavefield are wavefronts that converge towards the master station at anti-causal negative lapse times, refocus, and then diverge at causal positive lapse times (Wapenaar et al., 2005). The contribution from the isolated source is a wavefront that is excited at the isolated source at $\mathbf{r}_I$ at anti-causal lapse time $\tau = -|\mathbf{r}_m - \mathbf{r}_I|/c$ and that arrives at the master station at lapse time $\tau = 0$ s (Schippkus et al., 2022).

We use the terms causal and anti-causal to refer to positive and negative lapse times, respectively. In much of the interferometry literature, these terms are used synonymously to also express the direction of wave propagation: causal signals propagate away from the master station, anti-causal signals propagate towards it (Bensen et al., 2007; Roux, 2009; Wapenaar et al., 2010; Ermert et al., 2016). These two meanings are synonymous for a lapse-time symmetric C_1 wavefront induced by boundary sources. A C_1 wavefront excited by an isolated source, however, is not adequately described as propagating towards or away from the master station. Instead, it is more accurately described as propagating away from the isolated source.

Next, we describe a C_1 wavefield computed from field data and demonstrate how the conceptual framework of boundary sources and isolated sources helps explain the observations. Note that the distinction between boundary and isolated sources is merely conceptual but facilitates the synthesis of directivity effects.

2.1 Field data

We use field data recorded by a large-N ($N = 4907$) seismic deployment in the Vienna basin, Austria (Schippkus et al., 2022, Figure 2). Each station is equipped with

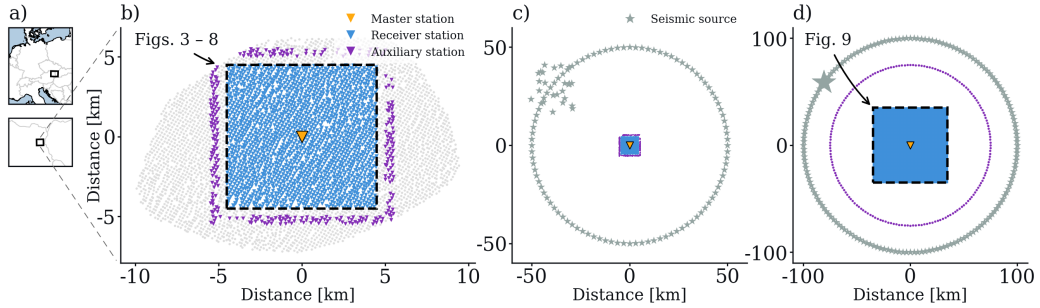

Figure 2. Station distribution and simulation configuration. (a) The overview map and the zoomed-in view show the Austrian-Slovakian border area of the data acquisition. (b) The map shows the spatial distribution of all stations (light gray dots) in the dataset, and the master station (orange triangle), receiver stations (blue triangles), and the auxiliary stations (purple triangles) used in this study are highlighted. (c) Configuration for the local wavefield simulations. The distribution of the synthetic sources (gray stars) are a combination of homogeneously distributed sources along a circle and additional isolated sources clustered in the Northwest. (d) The configuration of the far-field wavefield simulations involves a single strong isolated source in the Northwest.

12 or 24 10-Hz vertical-component geophones. The data are stacked on the hardware level to increase the signal-to-noise ratio, particularly at low frequencies. We select a subset of 1990 receiver stations in a square configuration, 304 auxiliary stations around the receiver stations, and a central master station (Figure 2b). These stations were deployed in March 2019 and recorded seismic noise for four weeks. We cut the records into non-overlapping 1 hr windows, apply spectral whitening (Bensen et al., 2007), compute cross-correlations between all receiver stations and the master station for all time windows, and stack the correlations of all time windows linearly to obtain the C_1 correlation wavefield.

Snapshots of the 0.3 Hz narrowband-filtered C_1 Rayleigh wavefield between the master station and the selected receiver stations at three lapse times $\tau = [-1, 0, 1]$ s show the effects of a non-isotropic energy flux that is associated with a non-homogeneous source distribution (Figure 3a–c). We choose 0.3 Hz for demonstration purposes because the coherent microseisms energy supports the reconstruction of clean C_1 wavefields. The corresponding ∼6 km wavelength is large compared to the ∼8 km array aperture, which does not support a clean illustration of propagation. The shortest inter-station distance is 190 m.

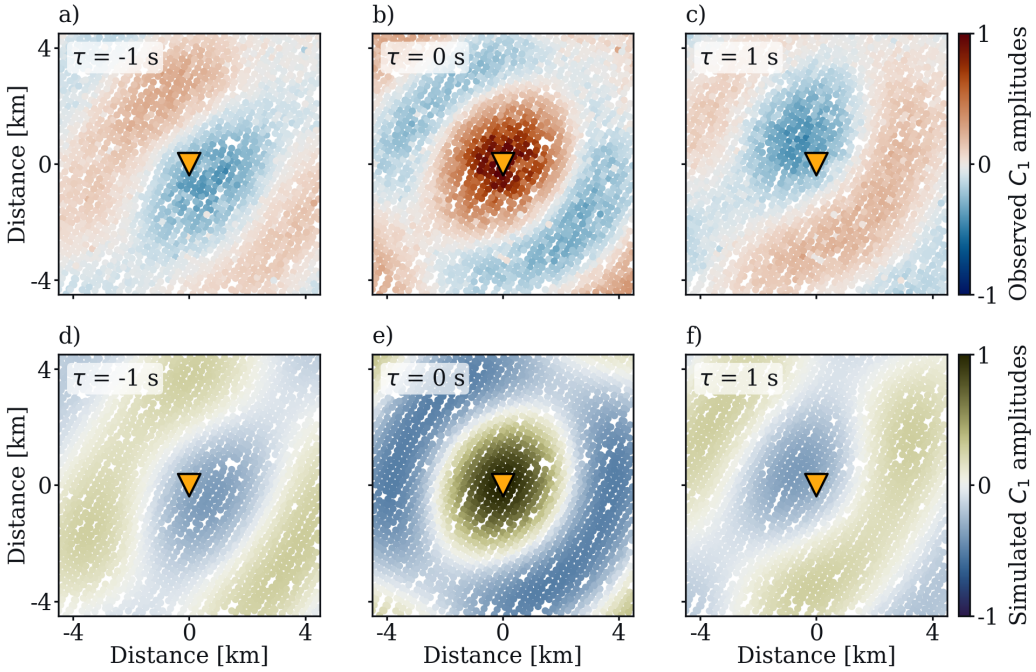

Figure 3. Snapshots of the 0.3 Hz narrowband-filtered C_1 correlation wavefield at three lapse times τ. (a–c) The C_1 correlation wavefield is estimated from field data. (d–f) The C_1 correlation wavefield is estimated from simulations. The observed lapse-time asymmetry is matched by the simulations that consider a directional illumination from the Northwest (Figure 2c).

However, this configuration convincingly resolves the amplitude fields at short distances including the focal spot at $\tau = 0$ s. We thus prioritize focal spot patterns instead of propagating far-field signals in our analysis and illustrations, but without loss of generality. For a homogeneous source distribution and an isotropic medium the narrowband focal spot takes the shape of a rotationally symmetric Bessel function in space and the correlation wavefield is lapse-time symmetric (Aki, 1957). Figure 3b shows a focal spot that is elongated in the Northeast-Southwest direction. This indicates an inhomogeneous source distribution (Ermert et al., 2016; Giammarinaro et al., 2023) that is oriented perpendicular to the axis of elongation, or, equivalently, parallel to the axis of shortening. The focal spot shape is π-symmetric with respect to the source location or flux direction. This direction, however, can be resolved from the lapse-time asymmetry of the correlation wavefield around the origin (Hillers et al., 2016) (Figure 3a, c).

In this area, wind turbines in a few hundred meters distance to the auxiliary stations in the Northeast of the deployment have been shown to act as isolated sources at

frequencies above 0.5 Hz (Schippkus et al., 2022). At 0.3 Hz, however, we find no evidence of significant influence of these wind turbines. Instead, the patterning of the obtained C_1 surface wavefield suggests isolated sources to the Northwest (Figure 3a–c). The excitation of secondary ocean microseisms (Ardhuin et al., 2015) is compatible with an isolated noise source, which induces C_1 wavefield components that are referred to as spurious arrivals (Snieder et al., 2008; Zeng & Ni, 2010; Retailleau et al., 2017; Schippkus et al., 2023; Safarkhani et al., 2025). Near the master station, this implies wavefield interference between the two C_1 components of the boundary sources and the isolated sources for all station pairs. The observed C_1 wavefield pattern is thus governed by the ocean microseisms sources in the Northern Atlantic Ocean (Kedar et al., 2008; Hillers et al., 2012; Juretzek & Hadziioannou, 2016).

2.2 Synthetic wavefields

To confirm this hypothesis, we simulate C_1 surface wavefields by first computing wavefield synthetics u (Equation 1) and then their cross-correlations. We model synthetic Green's functions analytically for a homogeneous acoustic medium, $G(\mathbf{r}_x, \mathbf{r}_s) = \exp\big(-i\omega t(\mathbf{r}_x, \mathbf{r}_s)\big)$, where $t(\mathbf{r}_x, \mathbf{r}_s)$ is the travel time between source and receiver. We neglect amplitude terms such as geometrical spreading or intrinsic attenuation. We do not expect amplitude effects to play a governing role in our observed C_1 wavefields reconstructions, hence, in our analysis, we focus on the phase characteristics of the correlation wavefields. Travel times are computed for a medium velocity of 1.9 km/s, estimated from the observed focal spot at 0.3 Hz. The velocity is constrained by a linear regression of the spatial autocorrelation data using a Bessel function model (Hillers et al., 2016; Tsarsitalidou et al., 2024). Our analytical simulation approach neglects the response of heterogeneous structure, but it effectively targets first-order source- and illumination-related effects.

We configure a source distribution that is compatible with the assumptions leading to Equation 3. Boundary sources are homogeneously distributed along a circle, and a cluster of isolated noise sources is located in the Northwest (Figure 2c) to model secondary ocean microseisms in the Northern Atlantic Ocean. For simplicity, we put these sources at ∼50 km distance compared to a more realistic ∼2000 km distance. This implies a small difference in the curvature of the wavefronts across the field and the synthetic array, but no feature in our results suggests a related bias. All sources are equiv-

alent, i.e., $N_I = N_s$. The source term N_s is a Ricker wavelet with 0.3 Hz peak frequency. We consider all sources uncorrelated as described in our implementation below.

The synthetic C_1 wavefield is the cross-correlation field of the simulated waveforms u. No additional pre-processing is applied. The C_1 wavefield is obtained by computing the correlation for each synthetic source individually and the correlations are stacked linearly to avoid correlation cross-terms between different sources (Wapenaar et al., 2010). The synthetic C_1 wavefield effectively reproduces the field data observations (Figure 3d–f). The remarkably high degree of similarity therefore suggests that the observed non-isotropic C_1 wavefield characteristic is a source-related phenomenon.

3 Higher-order correlation of direct waves (C_2)

We compute higher-order C_2 correlations of direct waves and investigate their sensitivity to source effects that are exposed in the C_1 wavefields. For homogeneously distributed sources, the direct waves in C_1 wavefields are propagating between the master and receiver stations (Equation 3, Figure 1a), i.e., the master station acts as a virtual source (Mehta et al., 2008). If several virtual sources are arranged homogeneously around the domain, the combination of these C_1 wavefields results in isotropic illumination (Figure 1b). Although the term virtual source can be helpful to communicate the physics, we advise caution about its application in the discussion of higher-order correlation phenomena. In the regular C_1 correlation procedure and context, the master station is interpreted to be the virtual source (Figure 1a). In the C_2 correlation procedure each auxiliary station is viewed as a virtual source for the C_1 computation (Figure 1b). In the final C_2 correlation wavefield stacked over all used auxiliary stations, however, the master station can again be addressed as the virtual source.

The higher-order C_2 correlation between a reference station at $\mathbf{r}_x$ and master station at $\mathbf{r}_m$, using auxiliary stations at $\mathbf{r}_a$ as virtual sources, is

$$C_2(\mathbf{r}_x, \mathbf{r}_m) = \langle C_1(\mathbf{r}_x, \mathbf{r}_a) C_1^*(\mathbf{r}_m, \mathbf{r}_a) \rangle_a \,. \tag{4}$$

Inserting Equation (2) yields

$$C_2(\mathbf{r}_x, \mathbf{r}_m) = \langle \langle u(\mathbf{r}_x) u^*(\mathbf{r}_a) \rangle_s \langle u^*(\mathbf{r}_m) u(\mathbf{r}_a) \rangle_s \rangle_a \,, \tag{5}$$

where $\langle \cdot \rangle_s$ indicates ensemble averaging over all original sources and $\langle \cdot \rangle_a$ indicates ensemble averaging over all auxiliary stations or virtual sources. This demonstrates that

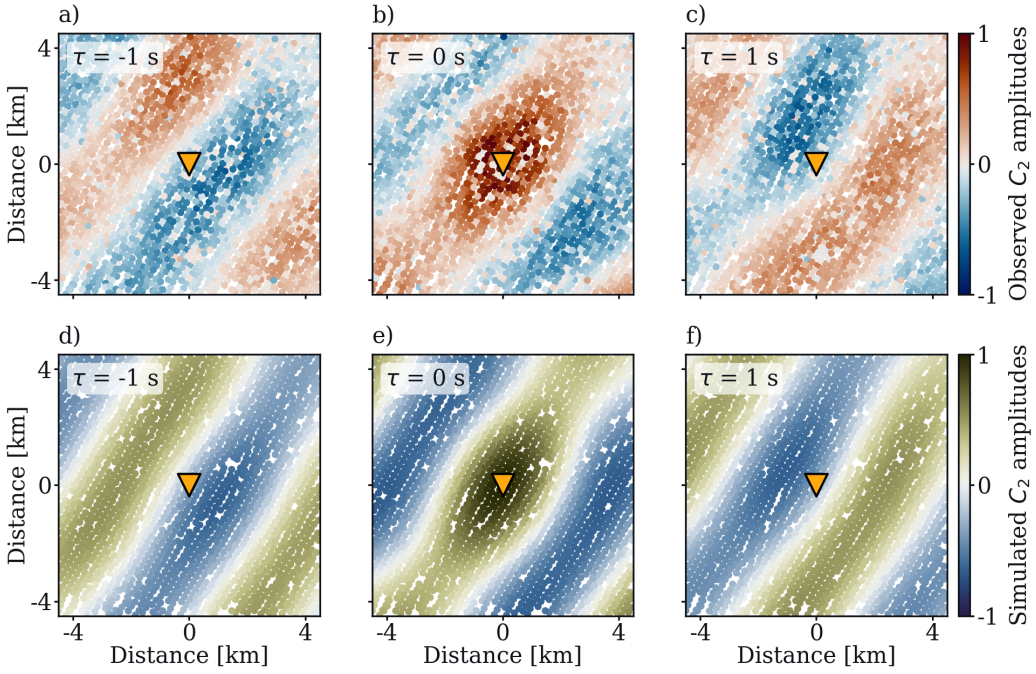

Figure 4. Snapshots of the 0.3 Hz narrowband-filtered higher-order C_2 correlation wavefield at three lapse times τ, averaged over all auxiliary stations. (a–c) The C_2 wavefield is estimated from field data. (d–f) The C_2 wavefield is estimated from simulations. In both cases, near-plane waves arriving from Northwest dominate the C_2 wavefield compared to the C_1 wavefield (Figure 3). The source effect of isolated ocean microseisms sources is amplified.

there are two mechanisms that introduce source effects and can affect the reconstruction of C_2 Green's functions: the distribution of original sources and the distribution of auxiliary stations.

We compute C_2 wavefields for the central master station and each receiver station from C_1 wavefields for all auxiliary stations and ensemble average over all obtained data (Figure 4). We treat the causal and anti-causal parts of the C_1 functions separately to avoid cross-terms, i.e., spurious arrivals that can emerge from the correlation between causal and anti-causal signals (Wapenaar et al., 2010). The C_2^+ wavefield from the causal part of the C_1 functions and the C_2^- wavefield from the anti-causal part are averaged for the C_2 wavefield (Sheng et al., 2018). We do not consider cross-component correlations—the correlation between causal and anti-causal parts of the C_1 wavefield—because one of the key characteristics of the effect of isolated sources on C_1 wavefields is the time-lapse asymmetry (Equation 3). Compared to the C_1 wavefield (Figure 3), the resulting

C_2 wavefield shows an amplified source effect both for field data and simulations (Figure 4). The obtained stronger azimuthal asymmetry is associated with yet stronger isolated sources in the Northwest, which results in a governing plane wave component across the array. In other words, the amplitude of the isolated-source wavefront in the C_2 wavefield is amplified relative to the boundary-source wavefront when compared to the C_1 wavefield. Note that this partitioning of isolated and boundary source contributions is therefore, to first order, insensitive to wave propagation effects acting on amplitude, such as intrinsic attenuation or geometrical spreading, because we neglect such amplitude terms in our simulations.

We use these wavefield simulation results to quantify the source effect induced by isolated sources (Figure 5). For this, we compute synthetic C_1 and C_2 wavefields for an ideal source scenario that excludes the isolated sources in the Northwest (Figure 2c). The C_1^{ideal} focal spot is a rotationally symmetric Bessel function in space (Figure 5a), as expected for isotropic illumination (Aki, 1957). The difference to the simulated C_1 wavefield including isolated sources (Figures 3e, 5b) then illustrates the source effect (Figure 5c). Amplitudes in the Northeast and Southwest quadrants are moderately increased, whereas amplitudes in the Northwest and Southeast quadrants show the opposite behavior. The comparison of the C_2^{all} focal spot (Figures 4e, 5e) with the C_2^{ideal} wavefield (Figure 5d), both averaged over all auxiliary stations, confirms that the source effect in the C_1 wavefield (Figure 5c) is amplified in the C_2 wavefield (Figure 5f). Again, the observed effects result from the local anisotropic flux, but are ultimately controlled by the source distribution. The imperfect distribution of auxiliary stations in this data set has its own weak effect on the wavefield shown in Figure 5g, but it does not govern the here discussed features. Last, in Figure 5h we compare the C_2^{all} focal spot against the C_1 reference observation that is, however, also affected by the flux directivity. In the next three sections we study the C_2 wavefield properties for three scenarios to understand the amplification of the directivity effect. The three scenarios include one original isolated source, homogeneously distributed boundary sources, and both source types combined.

3.1 C_2 properties for an isolated source

In the case of a single original source and a single auxiliary station, Equation 5 simplifies to

$$C_2(\mathbf{r}_x, \mathbf{r}_m) = u(\mathbf{r}_x)u^*(\mathbf{r}_m)|u(\mathbf{r}_a)|^2. \tag{6}$$

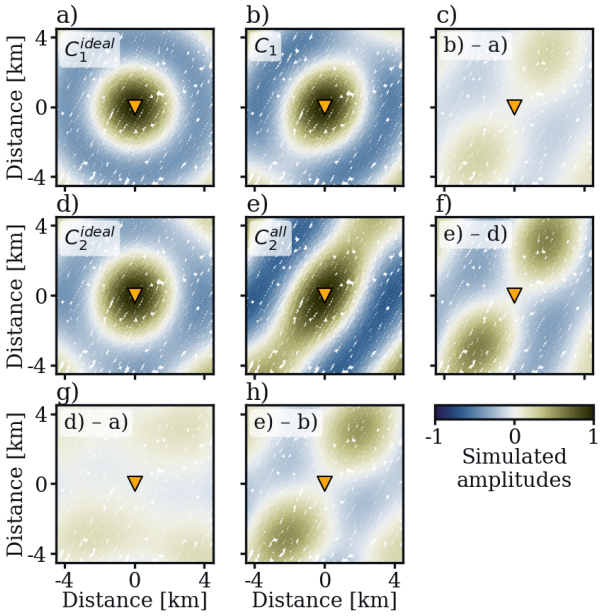

Figure 5. Synthetic focal spots illustrate source amplification effects. (a) The reference C_1^{ideal} focal spot for homogeneously distributed sources. (b) A C_1 focal spot in response to anisotropic illumination, as in Figure 3e. (c) The difference between the C_1 solution from panel (b) and the reference C_1^{ideal} from panel (a) illustrates the effect associated with the isolated sources added in the configuration in (b). (d) The C_2^{ideal} focal spot for the ideal source case averaged over all auxiliary stations. Weak azimuthal variations are controlled by the incomplete, square auxiliary station distribution (Figure 2b). (e) The C_2^{all} focal spot for anisotropic incidence averaged over all auxiliary stations, as in Figure 4e. (f) The source effect in the C_2 wavefield is amplified compared to the effect in the C_1 solutions in panel (c). (g) The amplitude effects that are controlled by the imperfect auxiliary station distribution are weak compared to the isolated source effect. (h) The difference between the C_2^{all} and the corresponding C_1 solutions indicates the amplification of the source effect in C_1 in panel (c).

Inserting Equation 1 yields

$$C_2(\mathbf{r}_x, \mathbf{r}_m) = \underbrace{|N_s|^2 G(\mathbf{r}_x, \mathbf{r}_s) G^*(\mathbf{r}_m, \mathbf{r}_s)}_{\text{isolated source in eq. 3}} \underbrace{|N_s|^2 |G(\mathbf{r}_a, \mathbf{r}_s)|^2}_{\text{influence of aux. station}} , \tag{7}$$

where the subscripts x, m, a, and s refer to the receiver station, master station, auxiliary station, and source, respectively. Only the first term carries phase information. This term is equivalent to the C_1 wavefield contribution of an isolated source for the same configuration (Equation 3), i.e., the phase is stationary with respect to the auxiliary sta-

tion (Sheng et al., 2018). The C_2 wavefield exhibits the wavefront excited by the isolated source, independent of the auxiliary station. We compute C_2 spatial auto-correlation wavefields for four different auxiliary stations to confirm the phase is stationary (Figure 6a–d). The observed weak differences in the spatial variation of the amplitudes across the four panels are related to the influence of the auxiliary station. This shows that C_2 wavefields associated with one isolated source but arbitrary auxiliary stations have the same phase characteristics. This further implies that averaging over different auxiliary stations, as we do for Figures 4 and 5, leads to constructive interference of the isolated source correlation wavefield contribution.

3.2 C_2 properties for boundary sources

When the original wavefield is excited by sources that are homogeneously distributed along a closed boundary S, the resulting C_1 and C_2 correlation wavefields behave differently compared to an isolated source. We refer to this as the "ideal" source case. The C_2 wavefield (Equation 4) for boundary sources is

$$C_2(\mathbf{r}_x, \mathbf{r}_m) = \oint_S C_1(\mathbf{r}_x, \mathbf{r}_a) C_1^*(\mathbf{r}_m, \mathbf{r}_a) d\mathbf{r}_s, \tag{8}$$

where integrating over the boundary sources accomplishes ensemble averaging. We apply the surface integral to both C_1 correlations separately and insert the boundary source contribution from Equation 2 to find

$$C_2(\mathbf{r}_x, \mathbf{r}_m) = \oint_S G(\mathbf{r}_x, \mathbf{r}_s) G^*(\mathbf{r}_a, \mathbf{r}_s) d\mathbf{r}_s |N_s|^2 \left(\oint_S G(\mathbf{r}_m, \mathbf{r}_s) G^*(\mathbf{r}_a, \mathbf{r}_s) d\mathbf{r}_s |N_s|^2 \right)^* . \tag{9}$$

Following Equation 11 of Wapenaar et al. (2005), the surface integrals resolve to

$$C_2(\mathbf{r}_x, \mathbf{r}_m) = \frac{\rho c}{2} |N_s|^2 [G(\mathbf{r}_x, \mathbf{r}_a) + G^*(\mathbf{r}_x, \mathbf{r}_a)] \left(\frac{\rho c}{2} |N_s|^2 [G(\mathbf{r}_m, \mathbf{r}_a) + G^*(\mathbf{r}_m, \mathbf{r}_a)] \right)^* . \tag{10}$$

We carry the complex conjugate $(\cdot)^*$ of the second term on the outside to avoid confusion about which Green's function terms relate to the causal and anti-causal parts of the C_1 wavefield. $G(\mathbf{r}_x, \mathbf{r}_a)$ and $G(\mathbf{r}_m, \mathbf{r}_a)$ correspond to the causal part of the C_1 wavefield, whereas $G^*(\mathbf{r}_x, \mathbf{r}_a)$ and $G^*(\mathbf{r}_m, \mathbf{r}_a)$ correspond to the anti-causal part. As said, we treat these parts separately to avoid correlation cross-terms. The C_2^+ wavefield from the

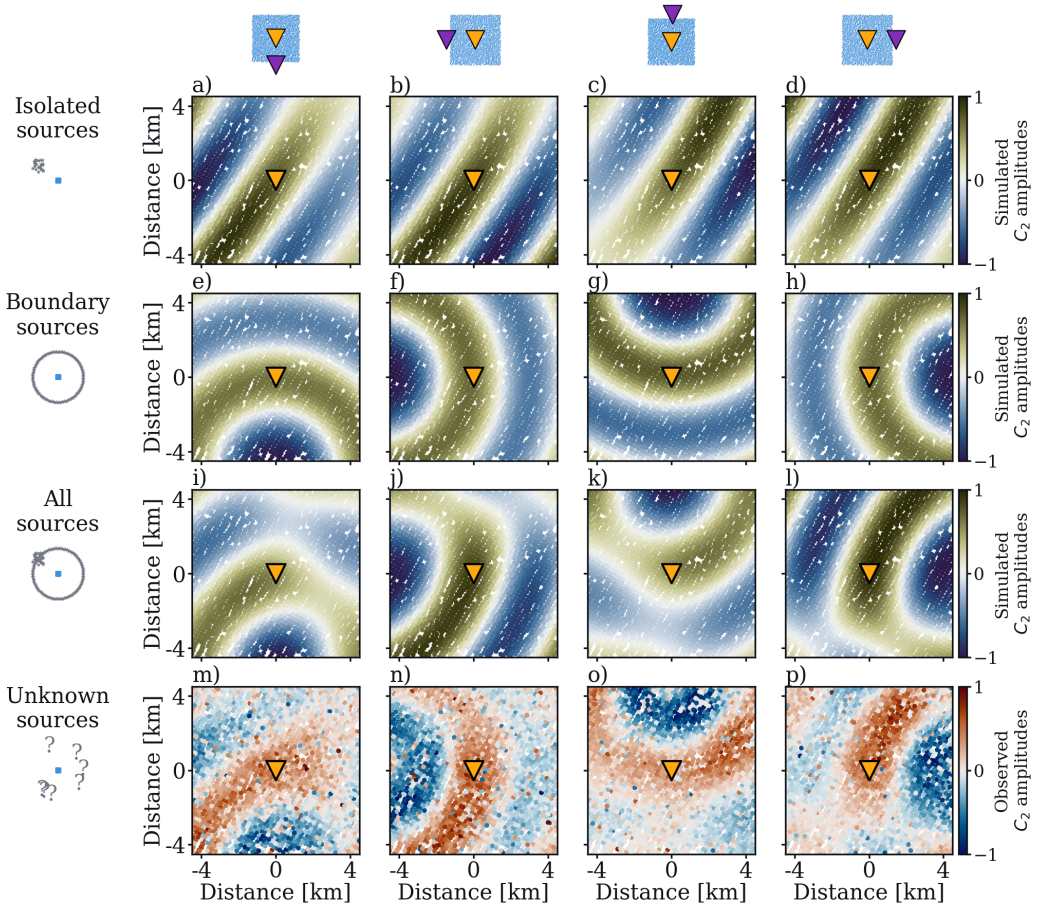

Figure 6. C_2 focal spots for (left to right) four single auxiliary stations and (top to bottom) four different excitation patterns. Cartoons at the top illustrate the purple indicated auxiliary station configurations. Cartoons on the left summarize the source configurations. (a–d) C_2 spatial auto-correlations in response to isolated sources or unidirectional incidence. The phase characteristics of the C_2 wavefield contributions controlled by the isolated sources are independent of the location of the auxiliary station. (e–h) For homogeneously distributed boundary sources the auxiliary station acts as virtual source. (i–l) The C_2 solutions for anisotropic incidence. The solution combines the patterns from the first and second row. (m–p) The C_2 focal spots obtained from field data exhibit a high degree of similarity to the synthetic results in row three, which implies a similar incidence pattern with a stronger excitation to the Northwest.

causal part of the C_1 wavefield, and the C_2^- wavefield from the anti-causal part are

$$C_2^+(\mathbf{r}_x,\mathbf{r}_m) = \left(\frac{\rho c}{2}\right)^2 |N_s|^2 \underbrace{|N_s|^2 G(\mathbf{r}_x,\mathbf{r}_a)G^*(\mathbf{r}_m,\mathbf{r}_a)}_{C_1(\mathbf{r}_x,\mathbf{r}_m) \text{ for a source at } \mathbf{r}_a \text{ (eq.3)}} \tag{11}$$

$$C_2^-(\mathbf{r}_x,\mathbf{r}_m) = \left(\frac{\rho c}{2}\right)^2 |N_s|^2 \underbrace{|N_s|^2 G^*(\mathbf{r}_x,\mathbf{r}_a)G(\mathbf{r}_m,\mathbf{r}_a)}_{C_1(\mathbf{r}_m,\mathbf{r}_x) \text{ for a source at } \mathbf{r}_a \text{ (eq.3)}} . \tag{12}$$

The phase of the C_2^+ and C_2^- wavefields for homogeneously distributed original sources and a single auxiliary station is equivalent to the phase of the C_1 wavefield for a single isolated original source for the same probing configuration. In other words, the auxiliary station acts as a virtual source for the C_2 wavefield reconstruction, similar to the role of an isolated source for C_1 (Equation 3). This differs from a C_2 wavefield in which the original wavefield is excited by an isolated source (Figures 6a–d), where the auxiliary station has no impact on the phase of the C_2 wavefield. C_2^+ and C_2^- are furthermore symmetric in lapse time, i.e., $C_2^+ = (C_2^-)^*$, unlike the asymmetric contribution of an isolated source (Equation 7). The source power spectrum $|N_s|^2$ now appears twice, which is not important for our narrowband investigations, but it is relevant for our analysis of broadband far-field wavefields discussed below.

We simulate the C_2 wavefield for this ideal source scenario, averaged over C_2^+ and C_2^-, to confirm that the auxiliary station acts as a virtual source in C_2 wavefields when the original sources are homogeneously distributed. The spatial auto-correlations in Figures 6e–h clearly show wavefronts that appear to be excited by the auxiliary stations in the South, West, North, and East, respectively.

3.3 C_2 properties for combined boundary and isolated sources

We argue that the observed C_1 and C_2 wavefield properties can be explained by a combination of boundary and isolated source effects. This conceptual framework adopted in the previous sections predicts the C_1 and C_2 wavefield amplitude patterns observed in the field data (Figures 3, 4). The patterns in Figure 6i–l demonstrate that the C_2 wavefield can be understood as a linear combination of the contributions from isolated and boundary sources for each auxiliary station. When the phase of the C_2 wavefield depends on the auxiliary station (Figures 6e–h), averaging over an azimuthally homogeneous auxiliary station distribution yields a correlation that approaches a rotationally symmetric Bessel function in response to isotropic illumination (Figure 5d). However, this applies only to the situation where the original source distribution is also homogeneous and thus the ambient flux isotropic. When the phase of the C_2 wavefield is instead stationary with respect to the auxiliary station as for isolated sources (Equation 7, Figure 6a–d), averaging over auxiliary stations amplifies this wavefield contribution. This mechanism governs our original observation of the amplified source effect in C_2 (Figure 4) compared C_1 (Figure 3).

We construct C_2 wavefields from field data for the four individual auxiliary stations (Figure 6m–p). The good agreement between the field data results in Figure 6m–p and the patterns in the corresponding panels in the row above indicates the efficiency of our source distribution concept. More generally, this good agreement shows that our conceptual framework of boundary and isolated sources is helpful in understanding the direction-dependent energy distribution and the resulting properties of higher-order correlations. However, this also implies a trade-off in the computation of higher-order correlations. On one hand, multiple auxiliary stations are required to yield symmetric C_2 wavefields even for isotropic illumination. The benefit of stacking contributions from many auxiliary stations is also indicated by the fairly poor signal-to-noise ratio obtained for a single auxiliary station (Figure 6m–p). On the other hand, each auxiliary station amplifies the effect of isolated sources further.

The isolated source distribution for our simulations is chosen to maximize the qualitative similarity between the synthetic C_1 and C_2 and the field data (Figures 3–6). We do not estimate the direction to and the strength or number of the contributing sources from the field data systematically because we focus on the first-order mechanisms that govern source effect amplification in higher-order correlations. A more quantitative approach to generate matching C_1 and C_2 synthetics can be developed from our results here. In reverse, such an approach can lead to the utilization of higher-order correlations for improved isolated source detection and characterization.

4 Auxiliary station distributions to mitigate C_2 wavefield asymmetry

The application of higher-order correlations serves two goals. It allows the use of asynchronously deployed stations for imaging and it can be a correlation wavefield enhancement technique to achieve better signal-to-noise ratio for more reliable measurements. Figure 4 illustrates the significantly amplified source effect for homogeneously distributed auxiliary stations, and Figure 6 shows the source effect in C_2 wavefields obtained with single auxiliary stations. Hence, averaging over all auxiliary stations is a suitable strategy only if the original source distribution is also azimuthally homogeneous. In practice, however, the distribution of stations that can be used as auxiliary stations is unlikely homogeneous, which can limit the data driven mitigation approach.

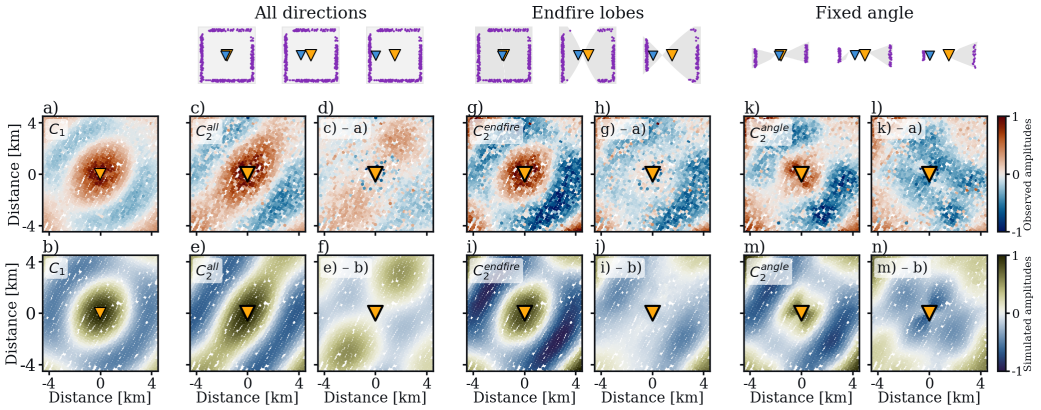

Figure 7. Influence of the auxiliary-station selection strategy on the source effect in C_2 wavefields. The cartoons sketch three receiver station examples (blue triangles) for the three auxiliary station (purple triangles) selection strategies. The gray area indicates the considered auxiliary station region. (a–b) The observed and simulated C_1 focal spots are reproduced from Figures 3b and 3d for reference. (c–f) C_2 focal spots for (c) field data and (e) simulations when auxiliary stations are located in all directions as in Figures 4, 5, as well as the (d, f) difference to the reference C_1 focal spots. (g–j) The effect of the endfire-lobe selection. The width of the selection area depends on inter-station distance. (k–n) The effect of the fixed-angle selection. We use $\pm 20^\circ$ relative to the inter-station azimuth. The variable observed focal spot characteristics controlled by the different selection strategies are well reproduced by the synthetic results for combined boundary and isolated sources.

Alternatively, auxiliary stations that are organized in line with each receiver-master station pair can be used to estimate C_2 Green's functions (S. Zhang et al., 2020; Nouibat et al., 2022). This strategy follows the same arguments that support the configuration of original sources located in line with station pairs for C_1 correlations, which is referred to as regions of stationary phase or endfire lobes (Snieder, 2004; Roux et al., 2004; Wapenaar et al., 2010). It has become clear, however, that the transfer of this argument from C_1 to C_2 wavefield reconstruction assumes a homogeneous original source distribution or isotropic illumination (Figure 6e–h).

Therefore, we investigate how the source effect associated with isolated sources affects C_2 solutions obtained with different selection strategies for station-pair-dependent auxiliary stations. For the selected stations to be in line with a receiver-master station pair, we can define endfire lobes (Roux et al., 2004) or a fixed-angle cone (S. Zhang et

al., 2020; Nouibat et al., 2022). We compare synthetic and observed C_1 wavefields with C_2 wavefields that are reconstructed with three auxiliary-station configurations that include stations in all directions, in endfire lobes, and in fixed-angle regions (Figure 7).

First, we select stations from all directions (Figure 7c–f). For comparison, we plot again the biased C_2^{all} focal spot estimated from field data (Figures 7c, 4b) and simulations (Figures 7e, 4e). The source effect relative to the C_1 wavefield we predict from simulations (Figures 7f, 5h) agrees well with the features in the C_2 field data correlations (Figure 7d). This confirms again that the all-directions strategy amplifies the C_1 wavefield source effect governed by the isolated sources.

Second, we select auxiliary stations from endfire lobes. Endfire lobes are simplified descriptions of source sensitivity kernels. We use equation (3) of Roux et al. (2004) to define their area

$$B(\delta\theta) = 1 - \frac{\delta\theta^4}{8}\left(\frac{|\mathbf{r}_m - \mathbf{r}_x|}{c}\right)^2\left(\omega^2 + \frac{\Delta\omega^2}{12}\right), \tag{13}$$

where B is the directivity pattern, $\delta\theta$ is the angle difference to the axis of the receiver-master station pair, $|\mathbf{r}_m - \mathbf{r}_x|$ is the distance between receiver and master station, c denotes the medium velocity, ω the central angular frequency, and $\Delta\omega$ the frequency bandwidth. The selections for three example receiver stations in the central section of Figure 7 illustrate that endfire lobes narrow with increasing distance between the station pair. We further limit the selection of endfire-lobe auxiliary stations to ensure the same number of auxiliary stations on both sides of every station pair to avoid any additional effect related to virtual source asymmetry. This asymmetry is related to different numbers of stations in the selection regions on each side. We average C_2 wavefields from the selected auxiliary stations and find that the resulting $C_2^{endfire}$ focal spots from field data (Figure 7g) and from simulations (Figure 7i) are characterized by an anisotropic amplitude distribution. They exhibit yet a different amplitude pattern (Figure 7h, j) compared to the pattern resulting from the all-directions stacking (Figure 7d, f).

Third, a further simplification of the endfire-lobe selection strategy is to define a cone with a fixed-angle opening and select auxiliary stations within that cone area. In contrast to the endfire-lobe strategy, the width of the selection area is independent of the inter-station distance. At short inter-station distances, this results in a significantly narrower selection area compared to the selection based on endfire lobes (Figure 7). An

auxiliary station is included if it satisfies equation (3) of S. Zhang et al. (2020)

$$||\mathbf{r}_a - \mathbf{r}_m| - |\mathbf{r}_a - \mathbf{r}_x|| \geq (1-\alpha)|\mathbf{r}_m - \mathbf{r}_x|, \tag{14}$$

where $\alpha = 1 - \cos(\theta)$ is the control on the opening of the cone and θ is half the opening angle. We choose $\theta = 20°$ (Nouibat et al., 2022). Similar to the endfire-lobe selection strategy, we also balance the number of auxiliary stations here. We note that for large inter-station distances, the endfire lobe areas and the fixed-angle cone areas can be similar. However, for the short inter-station distances compared to the ∼6 km wavelength here, the fixed-angle cones are much narrower (Figure 7). The resulting focal spots and amplitude patterns in Figure 7k–n show that at very short inter-station distances and in directions perpendicular to the Northwest-Southeast illumination additional amplitude variations are introduced compared to the endfire-lobe selection strategy.

None of the tested auxiliary station distributions fully mitigates the source effects observed in the C_1 wavefield to create an isotropic focal spot. Selecting auxiliary stations from all directions amplifies the amplitude pattern in the C_2 functions, and the patterns obtained with the endfire lobe and fixed angle configurations do similarly not show an improvement towards an isotropic distribution (Figure 7). This suggests that anisotropic flux cannot be corrected for by re-correlating direct waves. Consequently, the application of higher-order correlations of direct waves depends on the careful consideration of the imaging situation.

5 Impact on imaging

We address the impact of source effect amplification in higher-order correlations on passive imaging results by quantifying expected velocity measurement errors. We assess phase velocity estimates from correlation or focal spot data at local distances and group velocity measurements obtained from propagating waves that form the basis for surface-wave tomography. Investigating the two imaging approaches helps illustrate to what extent the insights we draw from our main focal spot analyses can apply to far-field tomographic investigations, the dominant imaging strategy in seismology. The comparison to a ground truth reference requires an analysis of these effects using simulations.

5.1 Phase velocity estimates from focal spot data for local imaging

The amplitude of the narrowband-filtered time domain focal spot or spatial autocorrelation field in a homogeneous medium for isotropic illumination is the classic SPAC result (Aki, 1957; Yokoi & Margaryan, 2008)

$$A(r) = J_0(kr) = J_0\left(\frac{\omega r}{c}\right), \tag{15}$$

where J_0 is the Bessel function of order zero, k is the wavenumber, c is the target phase velocity, and $r = |\mathbf{r}_x - \mathbf{r}_m|$ is the azimuthally independent distance between virtual source and receiver. We investigate the focal spots of the simulated ideal C_1^{ideal}, skewed C_1, all-direction-averaged C_2^{all}, endfire-lobe-averaged $C_2^{endfire}$, and fixed-angle-averaged C_2^{angle} solutions (Figure 8a–e).

We estimate the medium velocity c using a non-linear least squares regression between the time domain amplitude data and the isotropic J_0 parametrization (Figure 8f–j). For the regression, we use stations within 4.5 km distance to the master station, indicated by the dashed circles, to establish homogeneous azimuthal sampling. We do not account for a distance-dependent sample increase that can influence the sensitivity (Giammarinaro et al., 2023). The data range of $\sim 0.7\lambda$ emphasizes the local focal spot imaging approach (Giammarinaro et al., 2024; Tsarsitalidou et al., 2024).

We colorcode the simulated amplitudes in Figures 8f–j using the angle deviation of each station pair axis from the backazimuth to the isolated sources at $\mathbf{r}_I$ at N300°E. The panels illustrate the systematic amplitude effects governed by isolated sources described above. The reference medium velocity of 1.9 km/s is well recovered in the ideal C_1^{ideal} case, i.e., for homogeneously distributed sources that result in isotropic illumination (Figure 8f). This implies that a C_2^{ideal} focal spot too facilitates a low-error velocity estimate under the condition that the original sources and the auxiliary stations are distributed isotropically (Figure 5d). The skewed C_1 focal spot resulting from a combination of circularly arranged sources and additional isolated sources (Figure 8g) facilitates the recovery of the reference speed. This is compatible with numerical sensitivity tests that synthesize a similar illumination situation (Giammarinaro et al., 2023). In both cases, the complete azimuthal average using the isotropic J_0 model (Equation 15) results in an unbiased estimate (Aki, 1957). However, this entails that spatially variable focal spot sampling for reference stations located away from the array center, or for ir-

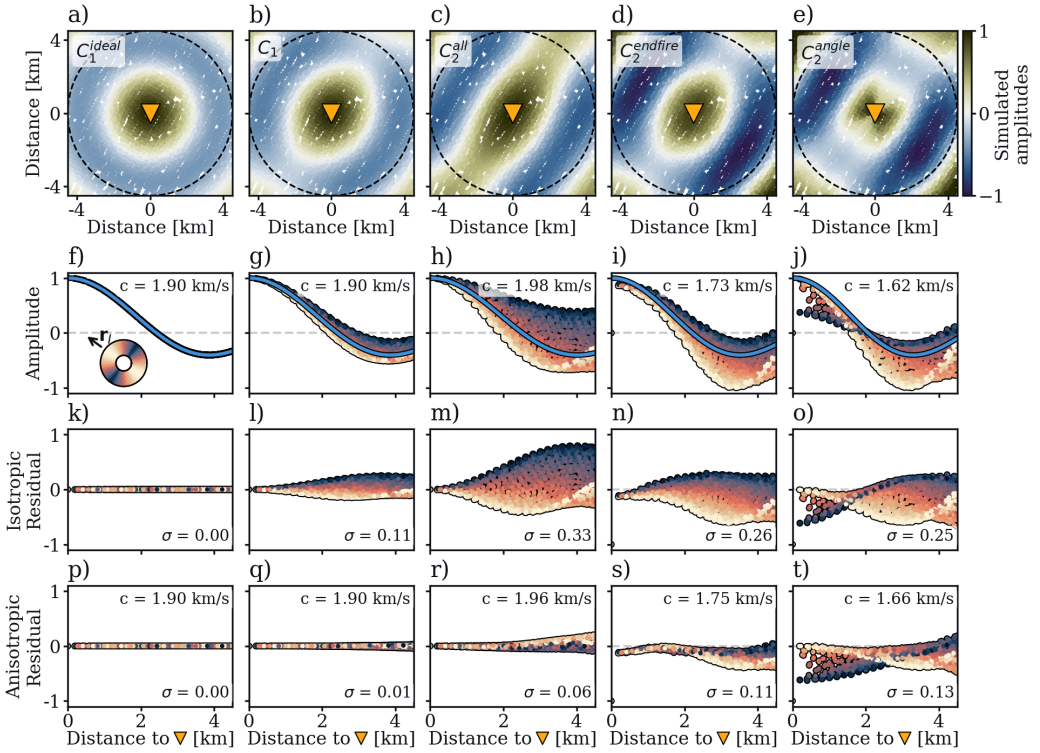

Figure 8. Impact of the source effect on focal spot regression results. (a–e) Simulated C_1^{ideal}, biased C_1, all-direction-averaged C_2^{all}, endfire-lobe-averaged $C_2^{endfire}$, and fixed-angle-averaged C_2^{angle} focal spots. We use stations within 4.5 km distance (dashed circles) for the regression to reduce potential azimuthal sampling artifacts. (f–j) The blue line shows the best-fitting isotropic J_0 model. The estimated phase velocity c is indicated. Samples are colored by the angle of the station pair axis relative to the direction towards the isolated sources at $\mathbf{r}_I$, indicated by the inset in panel (f). The reference velocity is 1.9 km/s. (k–o) Residuals of the isotropic model regression, σ is the associated standard deviation. (p–t) Residuals of focal spot regression results using a model parametrization that accounts for anisotropic illumination. The estimated phase velocity c is indicated.

regular array shapes, can yield inaccurate estimates that depend on the imaging configuration (Tsarsitalidou et al., 2022, 2026).

The three different auxiliary-station selection approaches for computing the C_2 wavefield produce different focal spot patterns (Figures 7e,i,m, 8c–e). These result in large velocity measurement errors up to 15% compared to the C_1 focal spot regression (Figure 8h–j) and significant amplitude residuals (Figure 8k–o). The C_2^{all} solution overes-

timates the reference velocity but yields a better result compared to the two sectorial strategies $C_2^{endfire}$ and C_2^{angle}, which both underestimate the velocity. This further indicates that the distribution of available auxiliary stations has a significant impact on the accuracy of the velocity estimate.

In addition, we estimate the medium velocity c using an anisotropic focal spot parametrization. The azimuthally dependent amplitude of the narrowband-filtered time domain focal spot in a homogeneous medium for anisotropic illumination is (Haney et al., 2012)

$$A(r,\psi) = a_0 J_0(kr) + \sum_{m=1}^{M-1} i^m J_m(kr)\big(a_m \cos(m\psi) + b_m \sin(m\psi)\big), \tag{16}$$

where a_0, a_m and b_m are weights, i is the imaginary unit, ψ is the angle between master and receiver station, and J_m is the Bessel function of the first kind and order m. We use only real-valued terms up to order 4, because $M = k_{\text{ang}} r_{\text{fit}} = \frac{2\pi}{\lambda} 0.7\lambda \approx 4.4$, where k_{ang} is the angular wavenumber and r_{fit} is the data range (Seydoux et al., 2017; Tsarsitalidou et al., 2026). Equation 16 then becomes

$$\begin{aligned} A(r,\psi) = a_0 J_0(kr) &- J_2(kr)\big(a_2 \cos(2\psi) + b_2 \sin(2\psi)\big) \\ &+ J_4(kr)\big(a_4 \cos(4\psi) + b_4 \sin(4\psi)\big). \end{aligned} \tag{17}$$

Figure 8p–t shows the resulting residuals between simulated focal spots and the anisotropic regression results, and the estimated medium velocity c is again indicated. Of course, the residuals are substantially reduced compared to the isotropic parametrisation (Figure 8k–o). However, the obtained velocity estimates are remarkably similar because of the azimuthal sampling. A complete azimuthal C_1 focal spot average for strongly directional or even unidirectional plane wave incidence yields an accurate velocity estimate (Aki, 1957; Giammarinaro et al., 2023; Tsarsitalidou et al., 2024), and for this case the isotropic and anisotropic model regressions are expected to yield the same results. This demonstrates that a large component of the effects we observe here can be modeled with SPAC concepts for anisotropic illumination (Nakahara, 2006; Haney et al., 2012). However, the remaining significant residuals, in particular for the two sectorial auxiliary-station configurations (Figure 8s,t), highlight the redistribution of energy in the spatial autocorrelation fields associated with the C_2 processing that is not considered by SPAC theory.

A resolution of this incompatibility involves the reconciliation of SPAC and iterative interferometry theories to account for the relative partitioning effects associated

with the original sources and the auxiliary stations. The AlpArray results from Tsarsitalidou et al. (2026) show that for synchronous arrays the anisotropic SPAC models of Nakahara (2006) and Haney et al. (2012) can resolve c estimates from C_1 focal spots. For synchronous acquisitions, this approach is then the recommended solution to mitigate azimuthally incomplete focal spot sampling and directional surface wave incidence. An advantage of higher-order correlations is the integration of asynchronously collected data. However, our results imply a limited usefulness of SPAC models for C_2 data regression considering the altered C_2 wavefield anatomy. For common in-situ anisotropic illumination situations, the advantage of higher-order correlations to utilize asynchronously collected data can thus be offset by yielding a biased estimate.

5.2 Group velocity estimates from Rayleigh wave propagation for tomography

In this work we have been focusing on the C_2 processing effects on the spatial autocorrelation field at near distances and on the implications for focal spot imaging. However, the dominant passive or correlation based imaging approach is ambient noise surface-wave tomography. We conclude our study by assessing the C_2 effects on surface wave propagation reconstructed at far-field distances, but we have to consider that our field data analysis is limited by the array aperture and the very short inter-station distances compared to the target microseisms wavelength (Figure 2). This wavelength is 6.3 km at the 0.3 Hz analysis frequency and all stations in the square array are thus located within approximately one wavelength. In ambient noise surface-wave tomography, station pairs with inter-station distances shorter than two wavelengths are commonly discarded to avoid the interference between the causal and anti-causal part of the C_1 wavefield (Bensen et al., 2007). The station configuration does therefore not support a data analysis of the C_2 effect on propagation at this frequency, hence we limit the analysis to simulated waveforms.

To avoid a separate discussion on isolated source characteristics at higher frequencies and shorter wavelengths, we adapt our simulation geometry and consider a larger domain with receiver stations in a square 70×70 km^2 grid with 500 m inter-station distance and place sources and auxiliary stations at larger distances. In Figure 2d, the 180 gray indicated boundary sources are organized on a circle with 100 km radius. One isolated source that is six times stronger than a boundary source is located in the North-

west of this circle. The choice of the isolated source strength is arbitrary, as long as it leads to an intended weak C_1 wavefield contribution that then dominates the C_2 wavefield after averaging over many auxiliary stations. How dominant an isolated source contribution appears in C_2 wavefields ultimately depends on its relative source strength and the number of auxiliary stations. The 180 purple indicated auxiliary stations are distributed evenly along a smaller circle with 75 km radius.

We simulate C_1, C_2^{all}, $C_2^{endfire}$, and C_2^{angle} wavefields as described above for this adapted simulation geometry and filter the waveforms between 0.2 and 0.4 Hz (Figure 9). The results in the second to fourth row of Figure 9 clearly illustrate the variable partitioning of the isolated and boundary source correlation wavefields that depends on the auxiliary-station selection strategy. The C_2 wavefield snapshots also show that higher-order correlations are characterized by the squared source power spectrum $|N_s|^4$ (Equations 7, 11, 12) compared to the $|N_s|^2$ power spectrum in C_1 (Figure 9a–c). For each correlation wavefield, we estimate group arrival times at the maxima of the waveform envelopes for each receiver-master station pair and convert that to group velocity. The resulting patterns of group-velocity errors are shown in the right column panels in Figure 9. Positive values indicate overestimates that we explain with the interference of the two wavefronts generated by the boundary sources and the isolated source that are illustrated in the three left columns. Schippkus et al. (2022) explain the emergence of this C_1 velocity bias pattern from interference.

Compared to the C_1 wavefield in the top row in Figure 9, all higher-order correlation wavefields shown in the other rows exhibit darker colors, indicative of larger amplitudes, for the isolated source wavefront that propagates across the array. The strongest amplification of the isolated source contribution relative to the circular boundary source component is observed for the all-direction auxiliary station configuration (Figure 9e–g). This results from averaging over significantly more auxiliary stations compared to the other two selection strategies. The group arrival times are then always measured on the wavefront excited by the isolated source because it has the largest amplitudes. For most receiver stations, this results in spurious low travel time estimates and high errors (Figure 9h). At the extreme, the velocity estimate at all stations that the isolated source wavefront reaches at $\tau = 0$ s (Figure 9f) approaches infinity. In contrast, we can make accurate estimates at receiver stations that are inline with the master station and the

isolated source. The correlation wavefield contributions of boundary and isolated sources are in phase along the white indicated region in Figure 9h.

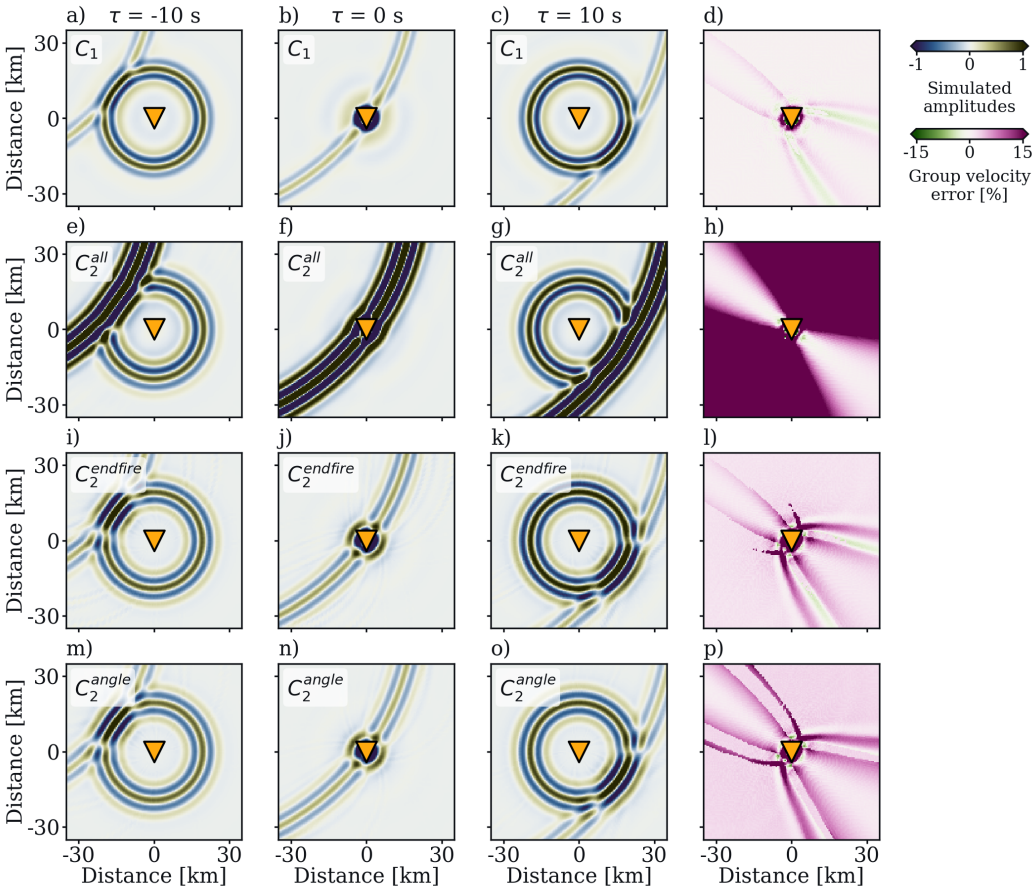

Figure 9. Impact of the isolated source or directional incidence effect on group velocity measurements using the configuration from Figure 2d. (a–c) The 0.2−0.4 Hz simulated C_1 wavefield. (d) The corresponding error of the group velocity estimates. The interference between different correlation wavefield contributions controls the typical bias pattern (Schippkus et al., 2022). (e–h) Simulated C_2^{all} solutions for the all-direction selection of auxiliary stations and the corresponding group velocity error. (i–l) Results for the endfire-lobe selection. (m–p) Results for the fixed-angle selection. All wavefield snapshots are normalised to their respective boundary source amplitude at stations in the top left quadrant at $\tau = 10$ s in panels (c), (g), (k), and (o). Panels (h), (l), and (p) show that all auxiliary-station selection strategies enhance the group velocity measurement bias associated with the source effects.

The endfire lobes and the fixed-angle cones configurations also induce enhanced velocity bias (Figure 9l, p). Because endfire lobes for large inter-station distances are fairly

narrow, the auxiliary stations selected with both strategies are similar in the far field, which results in the shown similar $C_2^{endfire}$ and C_2^{angle} wavefields in Figures 9i–k and 9m–o, respectively. This indicates that a fixed-angle configuration can be a valid strategy for propagation analysis. Note, though, that the two configurations yield different velocity errors, because the number of utilized auxiliary stations still varies. This results in systematically different relative weighting of the isolated source contribution.

Group velocity errors occur where the two wavefield contributions from isolated and boundary sources interfere. We show that this interference and these errors emerge already in the C_1 solutions (Figure 9a–d) and increase in the C_2 patterns (Figure 9e–p). Independent of the auxiliary station configuration, however, the phase of the boundary source contribution is accurately reconstructed in the C_2 wavefield. That is, C_2 contains the Green's function $G(\mathbf{r}_x, \mathbf{r}_m)$, here, the circular wavefront converging to and diverging away from the master station, in all cases. For strongly unidirectional illumination it is therefore possible to reduce the measurement bias by estimating velocities only from either the causal or anti-causal part of the C_2 wavefield. This utilizes the asymmetric lapse time contribution of isolated sources (Schippkus et al., 2022). At anti-causal lapse times the stations in the Southeast are unaffected by interference (Figure 9a, e, i, m), whereas stations in the Northwest are unaffected at causal lapse times (Figure 9c, g, k, o). Of course, this geometry depends on the relative position of the isolated sources and the direction of the energy flux.

Reducing the number of auxiliary stations mitigates the impact of the isolated sources, which is suggested by the observed smaller bias resulting from the endfire-lobe and fixed-angle configurations compared to the all-direction-averaging (Figure 9). However, the signal-to-noise ratio is poorer when averaging over fewer auxiliary stations and even a single auxiliary station does not eliminate the isolated source contribution in C_2 wavefields (Figure 6). Because the group-velocity errors are governed by the reconstructed wavefield interference, estimates of other wave properties including phase velocity or amplitude are similarly affected.

6 Discussion and conclusions

Non-homogeneous noise source distributions and the resulting directional surface wave incidence lead to incomplete approximations of the inter-station Green's functions

through cross-correlation. Various strategies (Sabra et al., 2005; Bensen et al., 2007; Seydoux et al., 2017; Fichtner et al., 2017; Sager et al., 2020; Schippkus et al., 2022; Giammarinaro et al., 2023) have been proposed to assess and mitigate the associated bias (Tsai, 2009; Froment et al., 2010; Wang et al., 2016; Schippkus et al., 2022) in the travel times estimates obtained from the C_1 noise correlation wavefield. In contrast to filtering and other invasive strategies, data driven approaches take advantage of the actual signal anatomy and statistics. Higher-order correlations or re-correlation is an alternative data-driven processing strategy for correlation wavefield enhancement (Stehly et al., 2008; Curtis & Halliday, 2010; Froment et al., 2011; Sheng et al., 2018) that offers the further advantage of integrating asynchronous records.

In this work we use data from a 2D seismic array that consists of nearly 5000 sensors and results from 2D acoustic numerical experiments to study properties of re-correlated wavefields. Our analysis is mostly based on time-domain spatial auto-correlations or focal spots, which differs from the conventional approach to study reconstructed propagating waves. This is motivated by the compact array size compared to the microseisms wavelength, but it demonstrates more generally the effectiveness of focal spot analysis for imaging and wavefield characterization. We find that the re-correlation of direct surface waves from C_1 solutions amplifies the effect of a non-homogeneous noise source distribution and hence directional incidence in the resulting higher-order C_2 correlations. The accuracy of medium velocity estimates from higher-order correlation wavefields can thus be significantly affected by the directional incidence (Figures 8, 9). We conclude that C_2 wavefields are a useful imaging resource, however, the re-correlation of direct waves is not an all-purpose correlation wavefield enhancement solution.

In addition to effects associated with the directional illumination, C_2 wavefields are sensitive to the configuration of auxiliary stations or virtual sources used for stacking (Figures 2, 6, 7). We test the selection of auxiliary stations from all directions, from endfire lobes, and from fixed-angle cones, which yield the C_2^{all}, $C_2^{endfire}$, and C_2^{angle} wavefields, respectively. All strategies yield isotropic C_2 wavefields in the case of homogeneously distributed original sources. However, they can not mitigate directional incidence effects. The persistent incidence effect is governed by C_2 wavefield contributions that are stationary in phase with respect to the auxiliary stations (Sheng et al., 2018, Equation 7, Figure 6a–d). This means that auxiliary stations have no influence on the reconstructed propagation of wavefronts induced by isolated sources in C_2 wavefields. When the orig-

inal sources are distributed homogeneously though, propagation does depend on the auxiliary stations and they can be considered as virtual sources (Figure 6e–h). Averaging over several auxiliary stations follows the necessity to improve the signal-to-noise ratio and achieve virtual source distributions that support seismic interferometry. This, however, amplifies the effects of isolated sources due to constructive interference.

In our synthetic far-field propagation experiments the reference wave velocity is accurately estimated only at stations located in line with the master station in the center and the isolated source in the Northwest (Figure 9). This likely explains why previous higher-order interferometry experiments have seemingly not been negatively affected by significant isolated source effects (Duguid et al., 2011; Curtis et al., 2012; Entwistle et al., 2015; S. Zhang et al., 2020; Nouibat et al., 2022). Source-receiver interferometry experiments, in particular, have been set up such that interference from sources at oblique angles is avoided and the correct phase information of earthquake signals is successfully reconstructed (Duguid et al., 2011; Curtis et al., 2012; Entwistle et al., 2015). S. Zhang et al. (2020) show that stacking over all auxiliary stations can result in significant spurious energy that is mitigated by selecting auxiliary stations only from endfire lobes. This is also in agreement with our analysis, that is, tuning the selection of auxiliary stations reduces the enhancement of isolated sources (Figure 9). The significant velocity errors, e.g., shown in Figure 9p, result from interference of the two C_2^{angle} wavefronts seen in Figures 9m–o that are excited by boundary sources and the isolated source, respectively. For stations in the Southwest and Northeast quadrants these wavefronts do not interfere. For these stations, setting constraints on realistic medium velocities can ensure that velocities are estimated from the correct wavefront (Nouibat et al., 2022) because wavefield contributions from isolated sources tend to appear as unrealistically fast spurious arrivals. In practice, only specific regions are affected negatively by the enhancement of isolated sources. For simple distributions of boundary sources and isolated source, these negative effects can be further avoided entirely by locating the isolated source and then estimating the speed either at the anti-causal or causal part of the C_2 wavefield depending on the station pair orientation (Figure 9), which is consistent with C_1 behavior (Schippkus et al., 2022). For our simulation configuration, stations in the Southeast are unaffected by interference at anti-causal lapse times (Figure 9e) and stations in the Northwest are unaffected at causal lapse times (Figure 9g). This also applies to the other C_1, C_2^{all}, and $C_2^{endfire}$ wavefields.

All C_2 wavefields have been obtained by stacking contributions from the causal and anti-causal parts of the C_1 wavefields. The rationale for this choice is twofold. First, we prefer consistent processing for all cases considered. Our analysis does not suggest that the discussed source effects are artifacts controlled by causal/anti-causal stacking. Second, we mostly focus on narrowband correlation wavefields at sub-wavelength distances and lapse time $\tau = 0$ s (Figures 3–8). The C_1 wavefront induced by boundary sources is lapse-time symmetric and is thus unaffected by causal/anti-causal stacking for all distances. The C_1 wavefront introduced by an isolated source also reaches the master station at lapse time $\tau = 0$ s and yields a signal on all stations within the array, too. At large distances, selecting either the causal- or anti-causal part of the correlation wavefield depending on the quadrant a station is in can avoid the isolated source bias, as described above. At short distances, the fact that all stations are affected by wavefield interference rules out this simple approach.

The three auxiliary-station selection strategies that we tested to constrain the local phase velocity using the shape of the C_2 focal spot yield inaccurate velocity estimates with errors up to 15% (Figure 8). The same inaccurate velocity estimates are obtained with the original isotropic SPAC model (Aki, 1957) and with the general formulation for anisotropic incidence (Nakahara, 2006; Haney et al., 2012), both applied to data from the full azimuthal range. The C_2 focal spots are thus not compatible with the model assumptions of SPAC theory. We recall the high similarity of observed and synthetic data illustrated in Figures 6 and 7 for various auxiliary-station configurations. It shows that the incompatibility is not controlled by our modeling approach, but the incompatibility is a genuine result of the applied C_2 processing. Neglecting the small difference in frequency content, Figure 9 shows the same wavefields on a 70×70 km^2 scale around the 9×9 km^2 focal spot area analyzed in Figure 8. Again, the $\tau = 0$ s refocusing panels illustrate the different amplitude scales of the circular and the curved wavefront associated with the circular source distribution and the isolated source, respectively. This partitioning is controlled by the auxiliary-station patterns. Together these results suggest that the C_1 configuration is equivalent to the time-reversed wavefield synthesized by Giammarinaro et al. (2023) using an amplitude distribution that varies smoothly with azimuth. In contrast, the enhancement of the unidirectional component through the C_2 processing then yields changes in the focal spot anatomy that are not built into the SPAC models. The significantly different focal spots in Figure 8c–e suggest that it is less ob-

vious to formulate simple geometry-based recommendations for auxiliary-station configurations to mitigate these effects. To make C_2 processing useful for focal spot imaging using asynchronously deployed stations the auxiliary-station effects have to be systematically integrated with SPAC concepts.

It has been demonstrated that the signal emitted by an active source is better reconstructed by iterative source-receiver interferometry compared to regular noise-based interferometry (Duguid et al., 2011). This is in direct agreement with our findings. Our results show that iterative interferometry enhances the reconstruction of signals from isolated sources with little sensitivity to the geometry of sources and receivers and the iterative interferometry strategy. In the case of source-receiver interferometry this is actually desired because the reconstruction goal is the isolated source signal, e.g., an earthquake or active source waveform (Curtis & Halliday, 2010; Duguid et al., 2011; Curtis et al., 2012; Entwistle et al., 2015). In the case of the here studied receiver-receiver interferometry targeted at structural imaging, the enhancement interferes with the goal to reconstruct the signal propagating between the two stations and not from an isolated source. In other words, both approaches are aimed at reconstructing Green's function but our results suggest that reconstruction via iterative interferometry based on isolated sources will yield more robust estimates as it suppresses rather than enhances interference artefacts. This approach is, however, limited in its applicability by the availability of isolated sources placed at useful locations. Our work demonstrates what biases to expect from iterative receiver-receiver interferometry in realistic scenarios, which is applicable to a significantly wider range of scenarios.

Higher-order correlations were introduced in the framework of C_3 wavefields that are obtained by the re-correlation of C_1 function coda waves (Stehly et al., 2008). For C_3, the multiple scattered coda waves are targeted to reduce potential source effects associated with inhomogeneous source distributions. Recent results indicate, however, that isolated noise sources with self-correlated source terms can induce spurious correlation wavefield contributions at late C_1 coda lapse times that are erroneously considered as random coda arrivals of scattered waves (Schippkus et al., 2023; Safarkhani et al., 2025). Such spurious C_1 wavefield contributions are likely similarly amplified in the higher-order correlations and thus influence the reconstructed ballistic waves. Our results imply that higher-order correlation is not an all-purpose mitigation strategy but an effective processing tool to analyze directional flux properties and the associated isolated sources. Ev-

ery iteration of higher-order correlation (Froment et al., 2011), e.g., adding another correlation step by re-correlating C_2 wavefields, further enhances the correlation wavefield contribution that is excited by isolated sources. This allows the targeted analysis of isolated sources, either to better characterize them, to utilize them, or for developing a strategy to mitigate their impact on imaging results.

Open Research

Data availability statement. To support reproducibility of our results, we provide all processing codes as Jupyter notebooks as well as the required data files. The data files are the linearly stacked C_1 cross-correlation functions computed from the raw field data and are available at Schippkus et al. (2025). The Jupyter notebooks implement all higher-order correlation processing, cover all wavefield simulations, and generate the figures and are available at Schippkus (2025).

CRediT author contributions. Conceptualization: SS, GH; Data curation: SS; Formal analysis: SS; Funding acquisition: SS, GH, CH; Investigation: SS; Methodology: SS, GH, CH; Resources: SS; Software: SS; Validation: SS; Visualization: SS; Writing – original draft: SS, GH; Writing – review & editing: SS, GH, CH.

Conflict of Interest statement. The authors declare that they have no conflicts of interest, financial or otherwise, that could have influenced the results or interpretation of this study. All sources of funding supporting this work are acknowledged in the manuscript, and there are no financial or personal relationships with other people or organizations that could inappropriately influence the results or reporting of this work.

Acknowledgments

The authors thank the reviewers Andrew Curtis and one anonymous for their constructive comments that helped improve the manuscript, as well as the editors Nori Nakata and Fenglin Niu. The authors further thank OMV E&P GmbH for access to the seismic data and permission to publish the correlation functions. The authors acknowledge funding provided by the European Union's Horizon 2020 research and innovation programme under the Marie Sklodowska-Curie grant agreement No. 955515 (SPIN-ITN, https://spin-itn.eu). This research was partially funded by the Federal Ministry of Education and Research (BMBF) and the Free and Hanseatic City of Hamburg under the Excellence Strat-

egy of the Federal Government and the Länder. This work was supported by the Research Council of Finland (Flagship of Advanced Mathematics for Sensing Imaging and Modeling grant 359182 and grant 322421).

References

Aki, K. (1957). Space and time spectra of stationary stochastic waves, with special reference to microtremors. *Bulletin of the Earthquake Research Institute*, *35*, 415–457. doi: http://hdl.handle.net/2261/11892

Ardhuin, F., Gualtieri, L., & Stutzmann, E. (2015). How ocean waves rock the Earth: Two mechanisms explain microseisms with periods 3 to 300 s. *Geophysical Research Letters*, *42*(3), 765–772.

Barmin, M. P., Ritzwoller, M. H., & Levshin, A. L. (2001). A fast and reliable method for surface wave tomography. *Pure and Applied Geophysics*, *158*, 1351–1375.

Bensen, G. D., Ritzwoller, M. H., Barmin, M. P., Levshin, A. L., Lin, F., Moschetti, M. P., ... Yang, Y. (2007). Processing seismic ambient noise data to obtain reliable broad-band surface wave dispersion measurements. *Geophysical Journal International*, *169*(3), 1239–1260. doi: 10.1111/j.1365-246X.2007.03374.x

Catheline, S., Benech, N., Brum, J., & Negreira, C. (2008). Time Reversal of Elastic Waves in Soft Solids. *Phys. Rev. Lett.*, *100*, 064301.

Chen, Y., & Saygin, E. (2020). Empirical Green's Function Retrieval Using Ambient Noise Source-Receiver Interferometry. *Journal of Geophysical Research: Solid Earth*, *125*(2), e2019JB018261. doi: 10.1029/2019JB018261

Curtis, A., Behr, Y., Entwistle, E., Galetti, E., Townend, J., & Bannister, S. (2012). The benefit of hindsight in observational science: Retrospective seismological observations. *Earth and Planetary Science Letters*, *345–348*, 212–220. doi: 10.1016/j.epsl.2012.06.008

Curtis, A., & Halliday, D. (2010). Directional balancing for seismic and general wavefield interferometry. *GEOPHYSICS*, *75*(1), SA1-SA14. doi: 10.1190/1.3298736

Derode, A., Larose, E., Campillo, M., & Fink, M. (2003). How to estimate the Green's function of a heterogeneous medium between two passive sensors? Application to acoustic waves. *Applied Physics Letters*, *83*(15), 3054-3056. doi:

10.1063/1.1617373

Duguid, C., Halliday, D., & Curtis, A. (2011). Source-receiver interferometry for seismic wavefield construction and ground-roll removal. *The Leading Edge*, *30*(8), 838–843. doi: 10.1190/1.3626489

Entwistle, E., Curtis, A., Galetti, E., Baptie, B., & Meles, G. (2015). Constructing new seismograms from old earthquakes: Retrospective seismology at multiple length scales. *Journal of Geophysical Research: Solid Earth*, *120*(4), 2466–2490. doi: 10.1002/2014JB011607

Ermert, L., Villaseñor, A., & Fichtner, A. (2016). Cross-correlation imaging of ambient noise sources. *Geophysical Journal International*, *204*(1), 347–364. doi: 10.1093/gji/ggv460

Fichtner, A., Stehly, L., Ermert, L., & Boehm, C. (2017). Generalized interferometry – I: Theory for interstation correlations. *Geophysical Journal International*, *208*(2), 603–638. doi: 10.1093/gji/ggw420

Fink, M. (1999). Time-reversed acoustics. *Scientific American*, *281*(5), 91–97.

Froment, B., Campillo, M., & Roux, P. (2011). Reconstructing the Green's function through iteration of correlations. *Comptes Rendus. Géoscience*, *343*(8-9), 623–632. doi: 10.1016/j.crte.2011.03.001

Froment, B., Campillo, M., Roux, P., Gouédard, P., Verdel, A., & Weaver, R. L. (2010). Estimation of the effect of nonisotropically distributed energy on the apparent arrival time in correlations. *GEOPHYSICS*, *75*(5), SA85–SA93. doi: 10.1190/1.3483102

Giammarinaro, B., Tsarsitalidou, C., & Hillers, G. (2024). Investigating the lateral resolution of the Rayleigh wave focal spot imaging technique using two-dimensional acoustic simulations. *Comptes Rendus. Géoscience*, *356*(S4), 41–57. doi: 10.5802/crgeos.254

Giammarinaro, B., Tsarsitalidou, C., Hillers, G., de Rosny, J., Seydoux, L., Catheline, S., ... Roux, P. (2023). Seismic surface wave focal spot imaging: Numerical resolution experiments. *Geophysical Journal International*, *232*(1), 201–222. doi: 10.1093/gji/ggac247

Haney, M. M., Mikesell, T. D., van Wijk, K., & Nakahara, H. (2012). Extension of the spatial autocorrelation (SPAC) method to mixed-component correlations of surface waves. *Geophysical Journal International*, *191*(1), 189–206. doi:

10.1111/j.1365-246X.2012.05597.x

Harmon, N., Gerstoft, P., Rychert, C. A., Abers, G. A., de la Cruz, M. S., & Fischer, K. M. (2008). Phase velocities from seismic noise using beamforming and cross correlation in Costa Rica and Nicaragua. *Geophysical Research Letters*, *35*(19). doi: 10.1029/2008GL035387

Hillers, G., Graham, N., Campillo, M., Kedar, S., Landès, M., & Shapiro, N. (2012). Global oceanic microseism sources as seen by seismic arrays and predicted by wave action models. *Geochemistry, Geophysics, Geosystems*, *13*(1). doi: 10.1029/2011GC003875

Hillers, G., Roux, P., Campillo, M., & Ben-Zion, Y. (2016). Focal spot imaging based on zero lag cross-correlation amplitude fields: Application to dense array data at the San Jacinto fault zone. *Journal of Geophysical Research: Solid Earth*, *121*(11), 8048–8067. doi: 10.1002/2016JB013014

Juretzek, C., & Hadziioannou, C. (2016). Where do ocean microseisms come from? A study of Love-to-Rayleigh wave ratios. *Journal of Geophysical Research: Solid Earth*, *121*(9), 6741–6756. doi: 10.1002/2016JB013017

Kedar, S., Longuet-Higgins, M., Webb, F., Graham, N., Clayton, R., & Jones, C. (2008). The origin of deep ocean microseisms in the North Atlantic Ocean. *Proceedings of the Royal Society A: Mathematical, Physical and Engineering Sciences*, *464*(2091), 777–793. doi: 10.1098/rspa.2007.0277

Lin, F.-C., Moschetti, M. P., & Ritzwoller, M. H. (2008). Surface wave tomography of the western United States from ambient seismic noise: Rayleigh and Love wave phase velocity maps. *Geophysical Journal International*, *173*(1), 281–298. doi: 10.1111/j.1365-246X.2008.03720.x

Lu, Y., Stehly, L., Paul, A., & the AlpArray Working Group. (2018). High-resolution surface wave tomography of the European crust and uppermost mantle from ambient seismic noise. *Geophysical Journal International*, *214*(2), 1136–1150. doi: 10.1093/gji/ggy188

Ma, S., & Beroza, G. C. (2012). Ambient-field Green's functions from asynchronous seismic observations. *Geophysical Research Letters*, *39*(6). doi: 10.1029/2011GL050755

Mao, S., Ellsworth, W. L., Zheng, Y., & Beroza, G. C. (2025). Depth-dependent seismic sensing of groundwater recovery from the atmospheric-river storms of

2023. *Science*, *387*(6735), 758–763. doi: 10.1126/science.adr6139

Mehta, K., Sheiman, J. L., Snieder, R., & Calvert, R. (2008). Strengthening the virtual-source method for time-lapse monitoring. *GEOPHYSICS*, *73*(3), S73-S80. doi: 10.1190/1.2894468

Nakahara, H. (2006). A systematic study of theoretical relations between spatial correlation and Green's function in one-, two- and three-dimensional random scalar wavefields. *Geophysical Journal International*, *167*(3), 1097–1105. doi: 10.1111/j.1365-246X.2006.03170.x

Nouibat, A., Stehly, L., Paul, A., Schwartz, S., Rolland, Y., Dumont, T., ... Cifalps Team, and AlpArray Working Group (2022). Ambient-Noise Tomography of the Ligurian-Provence Basin Using the AlpArray Onshore-Offshore Network: Insights for the Oceanic Domain Structure. *Journal of Geophysical Research: Solid Earth*, *127*(8), e2022JB024228. doi: 10.1029/2022JB024228

Poli, P., Campillo, M., Pedersen, H. A., & the POLENET/LAPNET Working Group. (2012). Body-wave imaging of earth's mantle discontinuities from ambient seismic noise. *Science*, *338*(6110), 1063–1065. doi: 10.1126/science.1228194

Retailleau, L., Boué, P., Stehly, L., & Campillo, M. (2017). Locating Microseism Sources Using Spurious Arrivals in Intercontinental Noise Correlations. *Journal of Geophysical Research: Solid Earth*, *122*(10), 8107–8120. doi: 10.1002/2017JB014593

Roux, P. (2009). Passive seismic imaging with directive ambient noise: Application to surface waves and the San Andreas Fault in Parkfield, CA. *Geophysical Journal International*, *179*(1), 367–373. doi: 10.1111/j.1365-246X.2009.04282.x

Roux, P., Kuperman, W. A., & the NPAL Group. (2004). Extracting coherent wave fronts from acoustic ambient noise in the ocean. *The Journal of the Acoustical Society of America*, *116*(4), 1995–2003. doi: 10.1121/1.1797754

Sabra, K. G., Gerstoft, P., Roux, P., Kuperman, W. A., & Fehler, M. C. (2005). Extracting time-domain Green's function estimates from ambient seismic noise. *Geophysical Research Letters*, *32*(3). doi: 10.1029/2004GL021862

Safarkhani, M., Schippkus, S., & Hadziioannou, C. (2025). Imprints of time-dependent microseism source distributions on the coda of correlations. *Geo-*

physical Journal International, *243*(2), ggaf358. doi: 10.1093/gji/ggaf358

Sager, K., Boehm, C., Ermert, L., Krischer, L., & Fichtner, A. (2020). Global-Scale Full-Waveform Ambient Noise Inversion. *Journal of Geophysical Research: Solid Earth*, *125*(4), e2019JB018644. doi: 10.1029/2019JB018644

Schippkus, S. (2025). *[Software] schipp/higher_order_correlations_c2: Pre-print.* Zenodo. Retrieved from `https://doi.org/10.5281/zenodo.17778709` doi: 10.5281/zenodo.17778709

Schippkus, S., Hadziioannou, C., & Hillers, G. (2025). *[Dataset] Large-N cross-correlation functions of ambient seismic noise recorded in the Vienna basin, Austria.* Center for Sustainable Research Data Management of the University of Hamburg, Germany. Retrieved from `https://doi.org/10.25592/uhhfdm.18152` doi: 10.25592/uhhfdm.18152

Schippkus, S., Safarkhani, M., & Hadziioannou, C. (2023). Continuous isolated noise sources induce repeating waves in the coda of ambient noise correlations. *Seismica*, *2*(2). doi: 10.26443/seismica.v2i2.499

Schippkus, S., Snieder, R., & Hadziioannou, C. (2022). Seismic interferometry in the presence of an isolated noise source. *Seismica*, *1*(1). doi: 10.26443/seismica.v1i1.195

Schippkus, S., Zigone, D., Bokelmann, G. H. R., & the AlpArray Working Group. (2018). Ambient-noise tomography of the wider Vienna Basin region. *Geophysical Journal International*, *215*(1), 102–117. doi: 10.1093/gji/ggy259

Sens-Schönfelder, C., & Wegler, U. (2006). Passive image interferometry and seasonal variations of seismic velocities at Merapi Volcano, Indonesia. *Geophysical Research Letters*, *33*(21). doi: 10.1029/2006GL027797

Seydoux, L., de Rosny, J., & Shapiro, N. M. (2017). Pre-processing ambient noise cross-correlations with equalizing the covariance matrix eigenspectrum. *Geophysical Journal International*, *210*(3), 1432–1449. doi: 10.1093/gji/ggx250

Shapiro, N. M., Campillo, M., Stehly, L., & Ritzwoller, M. H. (2005). High-resolution surface-wave tomography from ambient seismic noise. *Science*, *307*(5715), 1615–1618. doi: 10.1126/science.1108339

Sheng, Y., Nakata, N., & Beroza, G. C. (2018). On the Nature of Higher-Order Ambient Seismic Field Correlations. *Journal of Geophysical Research: Solid Earth*, *123*(9), 7969–7982. doi: 10.1029/2018JB015937

Snieder, R. (2004). Extracting the Green's function from the correlation of coda waves: A derivation based on stationary phase. *Physical Review E*, *69*(4 Pt 2), 046610. doi: 10.1103/PhysRevE.69.046610

Snieder, R., van Wijk, K., Haney, M., & Calvert, R. (2008). Cancellation of spurious arrivals in Green's function extraction and the generalized optical theorem. *Physical Review E*, *78*(3), 036606. doi: 10.1103/PhysRevE.78.036606

Stehly, L., Campillo, M., Froment, B., & Weaver, R. L. (2008). Reconstructing Green's function by correlation of the coda of the correlation (C3) of ambient seismic noise. *Journal of Geophysical Research*, *113*(B11). doi: 10.1029/2008JB005693

Toksöz, M. N., & Lacoss, R. T. (1968). Microseisms: Mode Structure and Sources. *Science*, *159*(3817), 872–873. doi: 10.1126/science.159.3817.872

Tsai, V. C. (2009). On establishing the accuracy of noise tomography travel-time measurements in a realistic medium. *Geophysical Journal International*, *178*(3), 1555–1564. doi: 10.1111/j.1365-246X.2009.04239.x

Tsarsitalidou, C., Giammarinaro, B., Hillers, G., & Boué, P. (2022). Anisotropic background illumination effects on focal spot imaging configurations with azimuthal asymmetry. In *AGU fall meeting abstracts* (Vol. 2022, p. S25E-0215).

Tsarsitalidou, C., Hillers, G., Giammarinaro, B., Boué, P., Stehly, L., & Campillo, M. (2024). Long Period Rayleigh Wave Focal Spot Imaging Applied to USArray Data. *Journal of Geophysical Research: Solid Earth*, *129*(5), e2023JB027417. doi: 10.1029/2023JB027417

Tsarsitalidou, C., Hillers, G., Stehly, L., Giammarinaro, B., Boué, P., & Paul, A. (2026). Rayleigh-wave focal spot imaging of the European Alps and surrounding areas. *Geophysical Journal International*, *245*(1), ggag017. doi: 10.1093/gji/ggag017

Wang, K., Luo, Y., & Yang, Y. (2016). Correction of phase velocity bias caused by strong directional noise sources in high-frequency ambient noise tomography: A case study in Karamay, China. *Geophysical Journal International*, *205*(2), 715–727. doi: 10.1093/gji/ggw039

Wapenaar, K., Draganov, D., Snieder, R., Campman, X., & Verdel, A. (2010). Tutorial on seismic interferometry: Part 1 — Basic principles and applications. *GEOPHYSICS*, *75*(5), 75A195-75A209. doi: 10.1190/1.3457445

Wapenaar, K., Fokkema, J., & Snieder, R. (2005). Retrieving the Green's function in an open system by cross correlation: A comparison of approaches (L). *The Journal of the Acoustical Society of America*, *118*(5), 2783–2786. doi: 10.1121/1.2046847

Yokoi, T., & Margaryan, S. (2008). Consistency of the spatial autocorrelation method with seismic interferometry and its consequence. *Geophysical Prospecting*, *56*(3), 435–451. doi: 10.1111/j.1365-2478.2008.00709.x

Zeng, X., & Ni, S. (2010). A persistent localized microseismic source near the Kyushu Island, Japan. *Geophysical Research Letters*, *37*(24). doi: 10.1029/2010GL045774

Zhang, S., Feng, L., & Ritzwoller, M. H. (2020). Three-station interferometry and tomography: Coda versus direct waves. *Geophysical Journal International*, *221*(1), 521–541. doi: 10.1093/gji/ggaa046

Zhang, X., Curtis, A., Galetti, E., & de Ridder, S. (2018). 3-D Monte Carlo surface wave tomography. *Geophysical Journal International*, *215*(3), 1644–1658. doi: 10.1093/gji/ggy362